

Confirmation of the spectral excess in DAMIC at SNOLAB with skipper CCDs

A. Aguilar-Arevalo,¹ I. Arnquist,² N. Avalos,³ L. Barak,⁴ D. Baxter,⁵ X. Bertou,³ I.M. Bloch,^{6,7} A.M. Botti,⁵ M. Cababie,^{8,9,5} G. Cancelo,⁵ N. Castelló-Mor,¹⁰ B.A. Cervantes-Vergara,¹ A.E. Chavarria,¹¹ J. Cortabitarte-Gutiérrez,¹⁰ M. Crisler,⁵ J. Cuevas-Zepeda,¹² A. Dastgheibi-Fard,¹³ C. De Dominicis,¹⁴ O. Deligny,¹⁵ A. Drlica-Wagner,^{5,12,16} J. Duarte-Campderros,¹⁰ J.C. D'Olive,¹ R. Essig,¹⁷ E. Estrada,³ J. Estrada,⁵ E. Etzion,⁴ F. Favela-Perez,¹ N. Gadola,¹⁸ R. Gaïor,¹⁴ S.E. Holland,⁷ T. Hossbach,² L. Iddir,¹⁴ B. Kilminster,¹⁸ Y. Korn,⁴ A. Lantero-Barreda,¹⁰ I. Lawson,¹⁹ S. Lee,¹⁸ A. Letessier-Selvon,¹⁴ P. Loaiza,¹⁵ A. Lopez-Virto,¹⁰ S. Luoma,¹⁹ E. Marrufo-Villalpando,¹² K.J. McGuire,¹¹ G.F. Moroni,⁵ S. Munagavalasa,¹² D. Norcini,¹² A. Orly,⁴ G. Papadopoulos,¹⁴ S. Paul,¹² S.E. Perez,^{8,9,5} A. Piers,¹¹ P. Privitera,^{12,14} P. Robmann,¹⁸ D. Rodrigues,^{8,9,5} N.A. Saffold,⁵ S. Scorza,¹⁹ M. Settimo,²⁰ A. Singal,^{17,21} R. Smida,¹² M. Sofo-Haro,^{5,22} L. Stefanazzi,⁵ K. Stifter,⁵ J. Tiffenberg,⁵ M. Traina,¹¹ S. Uemura,⁵ I. Vila,¹⁰ R. Vilar,¹⁰ T. Volansky,⁴ G. Warot,¹³ R. Yajur,¹² T-T. Yu,²³ and J-P. Zopounidis¹⁴

(DAMIC, DAMIC-M and SENSEI Collaborations)

¹ *Universidad Nacional Autónoma de México, Mexico City, Mexico*

² *Pacific Northwest National Laboratory (PNNL), Richland, WA, United States*

³ *Centro Atómico Bariloche and Instituto Balseiro,*

Comisión Nacional de Energía Atómica (CNEA),

Consejo Nacional de Investigaciones Científicas y Técnicas (CONICET),

Universidad Nacional de Cuyo (UNCUYO), San Carlos de Bariloche, Argentina

⁴ *School of Physics and Astronomy, Tel-Aviv University, Tel-Aviv, Israel*

⁵ *Fermi National Accelerator Laboratory, Batavia, IL, United States*

⁶ *Berkeley Center for Theoretical Physics, University of California, Berkeley, CA, United States*

⁷ *Lawrence Berkeley National Laboratory, Berkeley, CA, United States*

⁸ *Universidad de Buenos Aires, Facultad de Ciencias Exactas y Naturales,*
Departamento de Física, Buenos Aires, Argentina

⁹ *CONICET - Universidad de Buenos Aires, Instituto de Física de Buenos Aires (IFIBA), Buenos Aires, Argentina*

¹⁰ *Instituto de Física de Cantabria (IFCA), CSIC - Universidad de Cantabria, Santander, Spain*

¹¹ *Center for Experimental Nuclear Physics and Astrophysics,*

University of Washington, Seattle, WA, United States

¹² *Kavli Institute for Cosmological Physics and The Enrico Fermi Institute,*
The University of Chicago, Chicago, IL, United States

¹³ *LPSC LSM, CNRS/IN2P3, Université Grenoble-Alpes, Grenoble, France*

¹⁴ *Laboratoire de physique nucléaire et des hautes énergies (LPNHE),*

Sorbonne Université, Université Paris Cité, CNRS/IN2P3, Paris, France

¹⁵ *CNRS/IN2P3, IJCLab, Université Paris-Saclay, Orsay, France*

¹⁶ *Department of Astronomy and Astrophysics, University of Chicago, Chicago, IL, United States*

¹⁷ *C.N. Yang Institute for Theoretical Physics, Stony Brook University, Stony Brook, NY, United States*

¹⁸ *Universität Zürich Physik Institut, Zürich, Switzerland*

¹⁹ *SNOLAB, Lively, ON, Canada*

²⁰ *SUBATECH, Nantes Université, IMT Atlantique, CNRS-IN2P3, Nantes, France*

²¹ *Department of Physics and Astronomy, Stony Brook University, Stony Brook, NY, United States*

²² *Universidad Nacional de Córdoba, IFEG (CONICET) & RA0 (CNEA), Córdoba, Argentina*

²³ *Department of Physics and Institute for Fundamental Science,*

University of Oregon, Eugene, OR, United States

(Dated: June 5, 2023)

We present results from a 3.1 kg-day target exposure of two charge-coupled devices (CCDs), each with 24 megapixels and skipper readout, deployed in the DAMIC (DARK MATTER IN CCDs) setup at SNOLAB. With a reduction in pixel readout noise of a factor of 10 relative to the previous detector, we investigate the excess population of low-energy bulk events previously observed above expected backgrounds. We address the dominant systematic uncertainty of the previous analysis through a depth fiducialization designed to reject surface backgrounds on the CCDs. The measured bulk ionization spectrum confirms with higher significance the presence of an excess population of low-energy events in the CCD target with characteristic rate of ~ 7 events per kg-day and electron-equivalent energies of ~ 80 eV, whose origin remains unknown.

The DAMIC experiment searches for the interaction of dark matter particles in the galactic halo [1] with silicon atoms in the fully-depleted active region of sci-

entific charge-coupled devices (CCDs). Between 2017 and 2019, DAMIC acquired 11 kg-days of data with an array of seven CCDs with conventional readout (pixel

noise $\sigma_{\text{pix}} \sim 1.6 e^-$) installed in a low-background setup deep underground at SNOLAB [2]. In December 2020, DAMIC reported the presence of a statistically significant (3.7σ) excess of events above its background model between the threshold energy of 50 eV_{ee} and 200 eV_{ee} [2]. The population of the excess events was best described by ionization events uniformly distributed in the bulk of the CCDs, with an exponentially decaying energy spectrum with decay constant $\varepsilon = 67 \pm 37$ eV_{ee} and a rate of 5.1 ± 2.3 events per kg-day. The spectral fit was performed to all ionization events above the energy threshold in depth vs. energy space, with a full background model including different templates for bulk and surface events. This approach was necessary because the bulk and surface populations could only be distinguished statistically, since the determination of the depth of the interaction was limited by readout noise. Consequently, the dominant systematic uncertainty was identified as the modeling of the response of the CCDs to surface events, and the statistically significant rise was reported only as an unmodeled excess of events over background.

In November 2021, the DAMIC setup was upgraded with two skipper CCDs, which can achieve single-electron resolution through repeated non-destructive charge measurements (NDCMs) by means of a modified readout stage. This letter presents results from a 3.1 kg-day target exposure acquired throughout 2022 with the upgraded detector [3]. The order-of-magnitude improvement in readout noise—from $\sigma_{\text{pix}} \sim 1.6 e^-$ to $0.16 e^-$ —results in a significant improvement in the depth localization of ionization events. This allows for a new analysis based on a fiducial selection to obtain a clean sample of bulk events down to a threshold of 23 eV_{ee}. In addition, the lower threshold is expected to increase the measured rate of reconstructed excess events from 1.7 to 3.0 events per kg-day.

The DAMIC skipper upgrade features few notable differences from its predecessor [2]. The previous seven DAMIC CCDs were decommissioned to install two 24-megapixel DAMIC-M skipper devices [4] in a new oxygen-free high conductivity (OFHC) copper box. The stock copper was stored in SNOLAB for 5 years to suppress cosmogenic activation [5], and brought to the surface at the time of machining. The total sea-level exposure of the machined components is less than 9 days. The rate of backgrounds from the copper box is expected to be as low as in the previous installation. The box with the two CCDs is connected to the existing cold finger to bring the sensors to a temperature of $\lesssim 140$ K. The two ancient lead bricks employed in the previous installation are positioned above and below the CCD box to provide additional shielding from environmental backgrounds. CCD 1 is located at the bottom of the box, and CCD 2 at the top, with their front surfaces (on which the pixel array is patterned) oriented upward. There is a 2.5 mm vertical gap between CCDs, with no material in between. The previous vacuum interface board (VIB) was replaced with a new one designed for skipper devices,

which remains shielded by 18 cm of lead located above the CCDs [2]. CCD control and readout is performed with the Low Threshold Acquisition (LTA) electronics designed for SENSEI [6]. In the setup, two LTA boards are synchronized on the same clock signal allowing low-noise readout of both CCDs. The LTA readout is connected to the air-side of the new VIB via a 3 m cable with individual coaxial lines for each signal.

The 24-megapixel skipper CCDs were designed by Lawrence Berkeley National Laboratory (LBNL) [7] and fabricated by Teledyne/DALSA. The CCD substrate consists of 670 μm of fully-depleted, high-resistivity (>10 k $\Omega\cdot\text{cm}$) n-type silicon. Ionizing particles produce electron-hole pairs in the silicon as they lose energy. The charge carriers are drifted across the substrate, in the \hat{z} direction, by means of a bias voltage applied to a backside contact, $V_{\text{sub}} = 60$ V. As they drift in the substrate electric field, carriers experience thermal motion in the transverse plane ($\hat{x}\hat{y}$), whose variance is proportional to the transit time. Holes are collected in the overlying buried p-channel, which is separated from the three-phase polysilicon gates by an insulating layer. The polysilicon gates and ion-implanted channel stops define the pixel extent along the row (\hat{y}) and column (\hat{x}) directions, respectively. The pixels of DAMIC-M CCDs measure $15 \mu\text{m} \times 15 \mu\text{m}$. The full array consists of 6144×4128 pixels (columns \times rows), for a total sensitive mass of 8.9 g per CCD. After an exposure, clock signals sent to the polysilicon gates transfer the collected charge across CCD rows and into the horizontal register (bottom row), where it is clocked to two skipper amplifiers located at opposite ends (U and L) of the horizontal register. Skipper amplifiers can perform multiple NDCMs of the charge in a single pixel. Taking the average of N_{sample} pixel samples improves charge resolution by a factor $1/\sqrt{N_{\text{sample}}}$, which enables single charge resolution when using enough samples. Images are constructed from the order in which the pixels are read out. The energy depositions from low-energy ionizing particles—whose tracks are much shorter than the pixel size—result in pixelated 2D Gaussian distributions of charge in the images. The lateral spread of the charge distribution, σ_{xy} , is positively correlated with the depth of interaction, with a maximum value $\sigma_{\text{max}} \sim 1$ pix.

To minimize the leakage current in the CCDs, surface potentials were inverted to fill surface traps in several steps during the cool-down process, starting at 160 K until the final cold finger temperature of 110 K. CCD biases were optimized to suppress light emission by the amplifiers, and the clock values were selected to minimize spurious charge [8] while maintaining high charge transfer efficiency. Following commissioning and cool-down, the pixel readout noise for a single measurement (NDCM=1) was $\sim 4 e^-$ in all four skipper amplifiers. The background dark count rate was measured to be between 2.4×10^{-3} and $3.0 \times 10^{-3} e^-/\text{pix}/\text{day}$. The rate of accidental noise events, which sets the analysis threshold, depends on a combination of pixel readout

noise, shot noise from dark counts, and the exposure per pixel. While increasing the signal integration time and the number of NDCMs decreases the readout noise, it also increases the exposure per pixel. An increase in the exposure per pixel increases the dark counts per pixel, and hence the shot noise. We performed studies on simulated images with the measured noise profile of the CCDs to establish the readout parameters. For science data, CCDs were read out continuously with a signal integration time $t_{\text{int}} = 8 \mu\text{s}$ and 460 NDCMs per pixel.¹ This resulted in a pixel exposure time of ~ 50 hours, a pixel noise $\sigma_{\text{pix}} \sim 0.16 e^-$, and dark counts ranging between 4.0×10^{-3} and $35.0 \times 10^{-3} e^-/\text{pix}/\text{img}$. The output data were stored as arrays of size $3300 \times 210 \times 460$ ($N_{\text{columns}} \times N_{\text{rows}} \times N_{\text{NDCM}}$), with one file per amplifier. The CCD physical array is divided by two in the \hat{x} direction when the two amplifiers are used for readout. Each amplifier reads 3072 physical pixels per row. A total of 228 pixels per row were read out past the physical extent of the array in \hat{x} with each amplifier. This region of the output image is referred to as the overscan. Overscan pixels have significantly shorter exposure than physical ones, and allow a check on noise and charge transfer efficiency. Unlike previous DAMIC data runs, the charge was read out for every physical pixel, rather than after summing the charge from a group of pixels, since this provides better spatial resolution.

A total exposure of 4.8 kg-day was acquired between February 2022 and January 2023 in several data runs. For the first run, in which a 1 kg-day exposure was collected, images with a smaller overscan ($N_{\text{columns}} = 3100$) were acquired. Images were processed as follows. Images with pixel values in analog-to-digital units (ADUs) were constructed by averaging the value for each pixel across NDCMs. The first NDCM was excluded to avoid the noise transient at the start of pixel readout. This procedure produces a 3300×210 (3100×210) average image. The row median value was subtracted from each averaged pixel value on a row-by-row basis to correct for any baseline shift between rows. The distribution of averaged pixel values (PVD) exhibits discrete peaks corresponding to the pixel charge content ($0e^-$, $1e^-$, $2e^-$, etc.). The PVD of every image was fit to a Poisson distribution convolved with a Gaussian function to evaluate the gain (from the mean of the Gaussian, in ADU/e^-), noise (Gaussian standard deviation) and dark counts (the Poisson mean being the average charge per pixel per image). Forty average images were then concatenated into a joint 3300×8400 (3100×8400) image to reduce the number of ionization events split between images. Gain, noise, and dark counts were monitored during daily shifts, and individual images were visually inspected for hot regions and noise patterns. Any images showing unexpected behavior

were flagged and excluded from the analysis. Discarded images were generally found to be correlated with electrical power instabilities at SNOLAB. Images with gain outside the 3σ range defined for each amplifier and run were also excluded.

A mask was defined per amplifier to exclude defects and regions with increased dark counts. Defects in the silicon lattice alter the local bandgap, which leads to increased charge leakage at specific locations in the CCD [9]. Because of continuous readout, all defects appear as “hot” columns in the science run images. The average dark counts (λ_i) was measured for every column by performing a fit to the PVD from all images with a Poisson distribution convolved with a Gaussian function. Any columns with $\lambda_i > 35 \times 10^{-3} e^-/\text{pix}/\text{col}$ were excluded from the analysis. Columns with a charge distribution that is not Poisson, as estimated from a chi-square goodness-of-fit test to the PVD, were also excluded. Columns with $x > 1565$ in the 1L amplifier (L amplifier of CCD 1) were discarded due to inefficient charge transfer past this point, possibly due to a charge trap in the horizontal register. To maximize the sensitivity to defects, a set of images with NDCM=1 was acquired at a cold finger temperature of 160 K, where charge leakage from defects is orders of magnitudes larger. These “warm” images were read out after a 30-minute exposure of the pixel array, with defects appearing as localized hot pixels due to the relatively short readout time. Defects were identified in each warm image as contiguous pixels $> 5\sigma$ above the average pixel noise. In addition, we evaluated the median pixel value for every column over all images in the science data, and estimated a moving average of the column medians in a 200-column window. Any column in the science data with median value 1.3 times higher than the moving average and coincident with a defect in the warm images was excluded. Finally, to prevent the splitting of ionization events across the joint image edges, we masked a border of 10 pixels in the \hat{x} direction and 5 pixels in the \hat{y} direction around the joint image.

To remove backgrounds associated with high-energy ionization events, pixels were also masked on a per-image basis. Pixel clusters were identified as groups of contiguous pixels with charge $\geq 3 e^-$. The cluster energy was estimated as the sum of pixel values in the cluster assuming $3.8 \text{ eV}_{\text{ee}}/e^-$ [10]. For every cluster with energy $> 10 \text{ keV}_{\text{ee}}$, we masked the smallest rectangular region of pixels containing the cluster plus a 2-pixel wide border around it. To remove trailing charge from charge transfer inefficiencies, we also excluded the 800 (100) trailing pixels in the horizontal direction in the L (U) images, and 20 trailing pixels in the vertical direction. We observed $\mathcal{O}(10^{-4})$ cross talk between amplifiers, with high-energy events read out by one amplifier resulting in few-electron events in the other amplifiers. While this is most relevant for α decays, we conservatively masked all pixels that were read out at the same time as pixels within the rectangular box surrounding high-energy clusters. In addition, pixels for which the standard deviation

¹ Since the readout is continuous, the y coordinate of the image pixel does not correspond to the y coordinate of the event in the CCD pixel array.

of the NDCMs sample was larger than 10^5 ADU were excluded. This selection accounts for occasional inaccurate estimates of the pixel charge due to noise fluctuations.

The cluster search was performed using a likelihood clustering algorithm on the images [11]. The likelihood $\mathcal{L}(q_{ij}|N, \vec{\mu}, \sigma_{xy}, \lambda_i, \sigma_{\text{pix}})$ defines the probability that the pixel values q_{ij} in a specified window are described by a 2D Gaussian distribution of charge with mean position $\vec{\mu}$, lateral spread σ_{xy} , and amplitude N on top of shot noise with mean occupancy λ_i , where every pixel has white noise σ_{pix} . The images were scanned with a moving window of 5×5 pixels, where, at every window position, we computed the likelihood that pixels come only from noise ($\mathcal{L}_n : N = 0$) or noise plus a Gaussian charge distribution ($\mathcal{L}_g : N_0, \vec{\mu}_0, \sigma_{xy0}$). The initial guesses for N_0 and $\vec{\mu}_0$ are the total charge in the window and the center of the window, respectively. The initial guess for the lateral spread of the cluster size σ_{xy0} was set to 1.0 pix. The values for λ_i and σ_{pix} were fixed to the corresponding measurements for the specific image. At window positions where there is a clear preference for a Gaussian cluster ($\ln \mathcal{L}_g - \ln \mathcal{L}_n > 7$), we vary the window position until $\ln \mathcal{L}_g - \ln \mathcal{L}_n$ is maximized. We then fix the window and perform a log-likelihood optimization with N , $\vec{\mu}$, and σ_{xy} as free parameters. The test statistic $\Delta LL = -(\ln \hat{\mathcal{L}}_g - \ln \mathcal{L}_n)$, with $\hat{\mathcal{L}}_g$ the best-fit likelihood, is a metric for the preference of the Gaussian hypothesis, with more negative values corresponding to a higher probability of ionization event within the selected window. The best-fit values for N , $\vec{\mu}$, and σ_{xy} are taken as the best estimates for the energy, mean (x, y) position, and lateral spread of the cluster. To better estimate the shape of the cluster, a second fit was performed with σ_x and σ_y as independent free parameters. Only clusters where the fit window did not contain a masked pixel were considered for further analysis.

Additional criteria were applied to select ionization events with the expected 2D Gaussian topology. Clusters were discarded when the best-fit $\vec{\mu}$ was more than 1.2 pixels from the window center or the best-fit σ_x or σ_y were larger than $1.5 \sigma_{\text{max}}$. Ionization events interacting in the field-free regions past the horizontal register can produce horizontal clusters with degraded energy [12]. Such clusters were rejected by excluding events with $\sigma_y < 0.2$ and $\sigma_x > 0.5$ pix. We applied an analogous selection for vertical events, which can originate from charge released by traps in the CCD pixel array. Finally, to exclude clusters from transients of temporarily higher dark counts, we excluded reconstructed events below 1 keV_{ee} when more than 8% of pixels within ± 50 pixels about the center of the cluster along the row had a value $\geq 1 e^-$. The masks and selection criteria discussed so far result in a final exposure of 3.1 kg-days.

A selection on ΔLL was used to reject accidental clusters from noise. For this purpose, we simulated “blank” images, which contain only the measured readout noise per pixel and shot noise from dark counts as a function of column number. We ran the likelihood cluster-

ing on 30 kg-days of simulated blanks to get a distribution of accidental noise clusters, which had a maximum charge of $10 e^-$. We compared the distributions between data and blanks for clusters with $q \leq 10 e^-$ and $-25 < \Delta LL < -10$, where low-energy ionization clusters are expected to be sub-dominant. Excellent agreement in both cluster charge and the x coordinate of the cluster center was found. The accidental rate was chosen to be $R_{\text{noise}} < 0.01 (\text{kg-day})^{-1}$ across the charge range $[5, 10] e^-$. Table I reports the ΔLL selection under the requirement of equal contribution of noise accidentals from each charge bin. Above $10 e^-$, a fixed selection value $\Delta LL = -27.8$ was used.

Charge bin (e^-)	5	6	7	8	9	10
ΔLL selection	-27.2	-28.3	-28.9	-29.5	-30.8	-27.8

TABLE I. Selection on ΔLL in charge range $[5, 10] e^-$. Above $10 e^-$, a constant value $\Delta LL = -27.8$ was used.

The variance of the lateral diffusion of charges (the lateral spread of a low-energy event) can be modeled as [2]:

$$\sigma_{xy}^2(z, E) = -A \ln |1 - bz| \cdot (\alpha + \beta E)^2, \quad (1)$$

where z and E denote event depth and energy, respectively, and parameters A and b depend on the microscopic properties of the substrate at operating temperature and V_{sub} . Best-fit values for the parameters $A = 3.07 \text{ pix}^2$ and $b = 5.35 \times 10^{-4} \mu\text{m}^{-1}$ were obtained in a surface setup using straight cosmic muon tracks [11]. The values of $\alpha = 0.889$ and $\beta = 7.4 \times 10^{-3} \text{ pix/keV}_{ee}$ were obtained from a fit to σ_{max} as a function of energy in the SNOLAB data. To remove ionization events originating from the surfaces of the CCDs, we performed a selection on σ_{xy} as a function of energy. We simulated events originating $< 10 \mu\text{m}$ from the front and back surfaces according to the diffusion model and added them uniformly in (x, y) on blank images. We ran the likelihood clustering on the images to obtain the response of the CCD to surface events and identified the σ_{xy} values as a function of energy that rejected 95.4% of simulated surface events. This selection was validated over the full energy range in the surface laboratory by illuminating with a ^{14}C pure-beta source ($Q_\beta = 156.476 \text{ keV}$) the front and the back sides of a CCD from the same batch as those installed at SNOLAB. The CCD was operated with the same parameters, readout settings and dark counts as in SNOLAB. The fraction of events retained after 95.4% (2σ) bulk fiducial selection was $4 \pm 1\%$ and $3 \pm 1\%$ for backside and frontside illumination, respectively.

To estimate the selection efficiency for bulk events after noise- and surface-event rejection, we simulated ionization events uniformly distributed in z on blank images and reconstructed them with likelihood clustering. Fig. 1 shows the efficiency of the ΔLL and σ_{xy} selections for valid clusters. The ΔLL selection allows efficient recon-

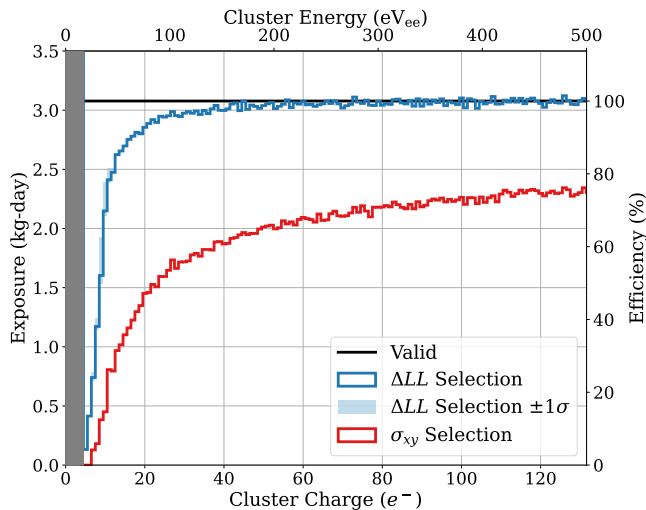


FIG. 1. Selection efficiency of simulated clusters after noise (blue line) and surface-event (red line) rejection. The horizontal black line shows the exposure for valid clusters. The gray area below 23 eV_{ee} marks the energy range below the analysis threshold.

struction ($\epsilon \geq 10\%$) of low-energy clusters down to $6e^-$ (23 eV_{ee}), which we set as the analysis threshold.

Although the copper box and CCD packages of the upgraded detector have a different geometry than in the previous installation, the apparatus components and their materials (*i.e.*, CCDs, Kapton flex cables, glue, OFHC copper, brass screws, and ancient lead) remain nominally the same. To confirm that the ionization spectrum features the same dominant background components as before, we first analyzed the spectrum above 0.5 keV_{ee}, where no excess above the background model was previously observed. The overall (bulk) background rate in the 1–6 keV_{ee} energy range of 9.7 ± 0.8 (4.4 ± 0.6) keV_{ee}⁻¹ kg⁻¹ day⁻¹ is comparable to the previous installation [2]. A spectral analysis up to 20 keV_{ee} showed the characteristic spectrum of cosmogenic tritium ($Q_\beta = 18.592$ keV) in the bulk of the CCDs over an approximately constant background from Compton scattering of external γ rays. Surface events and X-ray lines from ²¹⁰Pb decays on the CCD surfaces were also identified with comparable rates as before.

After establishing the final cluster selections and performing background studies, we unblinded the region of interest (ROI) below 0.5 keV_{ee}. The clusters retained after the ΔLL selection are shown in Fig. 2, with energy and σ_{xy} projections beside the corresponding axes. The σ_{xy} projection shows the distribution of all ionization events from threshold to 1.0 keV_{ee}, while the energy projection shows the spectrum of bulk events after σ_{xy} selections, demarcated by the black dashed lines in the 2D plot. Clusters in the ROI were individually inspected and were found to have the expected topology, to be located away from masked regions of the CCD, and not spatially correlated with other ionization events. The event

(x, y) and time distributions were confirmed to be statistically consistent with uniformity, with Kolmogorov-Smirnov p-values between 0.36 and 0.78. The σ_{xy} distribution of clusters in the ROI was found to be consistent with the three distinct populations of bulk, front- and back-surface events. A total of 15 events pass the fiducial σ_{xy} selection in the ROI, in contrast with the 4.8 ± 0.7 expected from the background rate measured in the 1–6 keV_{ee} range. The increasing rate of events toward low energies at large σ_{xy} is caused by partial charge collection of ionization events in the backside of the CCD, as described in Ref. [2].

Our background model [2] predicts an approximately constant spectrum of bulk events at low energies. This is expected since electronic recoils can only be induced in the bulk by β decays or Compton scatterings, which both have approximately flat spectra in the ROI.² Nuclear recoils from fast neutrons are expected to have orders-of-magnitude lower rates [2]. We thus performed an extended unbinned likelihood fit to the energy spectrum of bulk events with a flat background component and an exponentially decaying spectrum, which adequately parametrized the observed excess in the previous analysis. The free parameters in the fit are the integrated counts in the background (b) and excess (s) spectra, and the decay energy (ϵ) of the exponential. The spectra were corrected for the bulk event acceptance in Fig. 1 and the fit was performed between 0 and 6 keV_{ee}. The results are shown in Fig. 3 for $E < 1$ keV_{ee}. The fit finds $s = 12.3 \pm 3.9$ excess events with $\epsilon = 89 \pm 30$ eV_{ee}, and $b = 68.7 \pm 8.5$ background events, corresponding to 4.9 ± 0.6 background events in the ROI. A likelihood ratio test between the best fit and a background-only ($s = 0$) fit rejects the background-only hypothesis with a p-value of $p = 3.54 \times 10^{-8}$ (5.4σ). Based on the number of events rejected by the σ_{xy} selection, we expect 1.7 ± 0.3 leakage events from the surface in the ROI. We correct the number of bulk excess events by subtracting the expected leakage from s , and translate to a total rate of 9.4 ± 3.5 per kg-day from the fiducial exposure. The parameter space of the measured excess compared to the result from the previous 11 kg-day exposure [2] is shown in Fig. 4. The two results are statistically compatible and suggest a common origin of the excess population.

In summary, an excess population of bulk events above the expected background spectrum has been observed in two independent setups of DAMIC at SNOLAB, which employed CCDs with significantly different noise characteristics and readout modes. Both CCDs with conventional [15] and skipper [13] readout have demonstrated the capability to correctly resolve spectral features at the

² The Compton scattering spectrum in silicon is approximately flat between 500 eV and 200 eV, it drops by 50% between 200 eV and 100 eV, and then plateaus [13]. This results in an up to 25% decrease in the background rate below 200 eV_{ee}, equivalent to only 5% of the total spectrum. See Fig. 3.

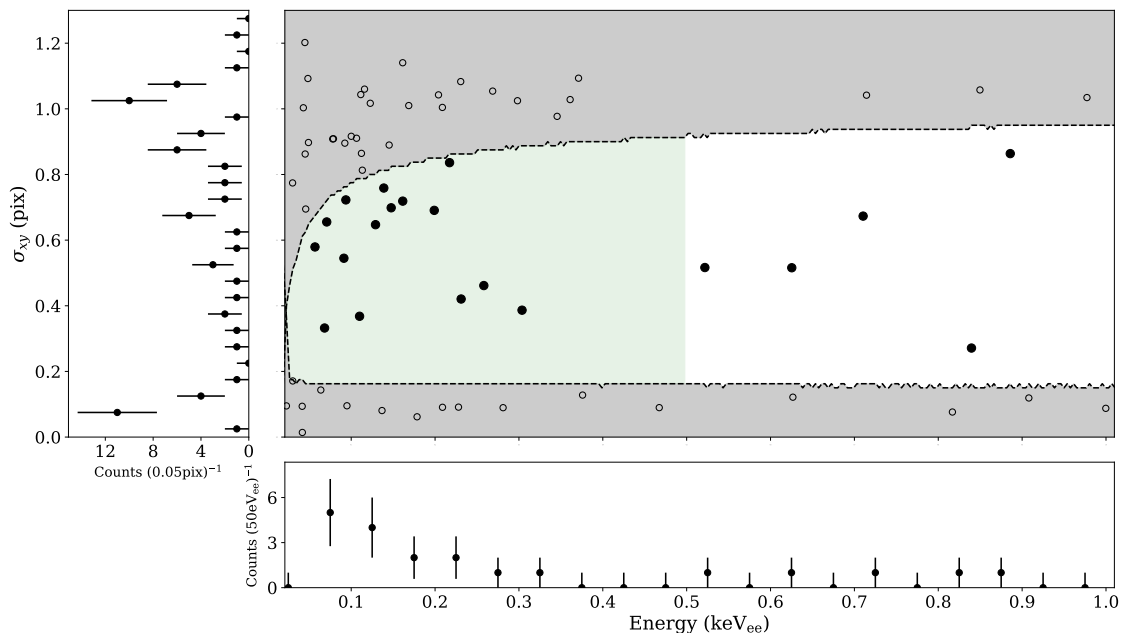


FIG. 2. Distribution of clusters in energy vs. σ_{xy} space, for $E \in [0.023, 1]$ keV_{ee}. Clusters with large (small) σ_{xy} correspond to events occurring in the back (front) of the CCDs. Grey regions are excluded by the 95% surface event rejection, which results in the final sample of bulk events (filled circles). The green-shaded region represents the energy ROI ($E < 0.5$ keV_{ee}) for bulk events. The left (bottom) panel shows the σ_{xy} (energy) projection of all (bulk) events.

energies where the excess is observed. The topology of the events—which can be resolved with high resolution thanks to the sub-electron noise of skipper CCDs—is consistent with ionization events. The modeling of the CCD response to surface events, which was the dominant systematic uncertainty in the previous analysis, has been addressed by analyzing a clean sample of bulk events se-

lected using the lateral spread of the clusters (σ_{xy}). The efficiency of this selection was directly validated with a radioactive-source calibration in the laboratory.

The observed excess ionization events likely arise from an unidentified source of radiation in the DAMIC detector or from the environment, which is common to the two experiments. The only known interactions that could give rise to the observed excess spectrum are those from neutrons with silicon nuclei in the bulk of the CCDs. The observed spectrum would require neutrons with energies up to ~ 17 keV and a flux of ~ 0.2 cm⁻²d⁻¹ through the CCDs. No such source of neutrons has been identified. Turning to more exotic interpretations, the bulk excess spectrum is well described by nuclear recoils from interactions of weakly interacting massive particles (WIMPs). For spin-independent WIMP-nucleus coherent elastic scattering with standard galactic halo parameters [16], the excess corresponds to a WIMP with mass ~ 2.5 GeV/ c^2 and a WIMP-nucleon scattering cross section $\sim 3 \times 10^{-40}$ cm². This interpretation is nominally excluded by results from CDMSlite [17] and DarkSide-50 [18]. Attempts to find a consistent interpretation between these experiments by systematically varying detector response (e.g., nuclear-recoil ionization efficiencies), WIMP speed distribution, as well as alternate particle interaction models (e.g., Ref. [19]) are beyond the scope of this letter.

The SENSEI experiment [20], currently taking data at SNOLAB, is designed to acquire a larger exposure of ~ 40 kg-day with skipper CCDs and similar backgrounds to DAMIC at SNOLAB in 2023-2024. The

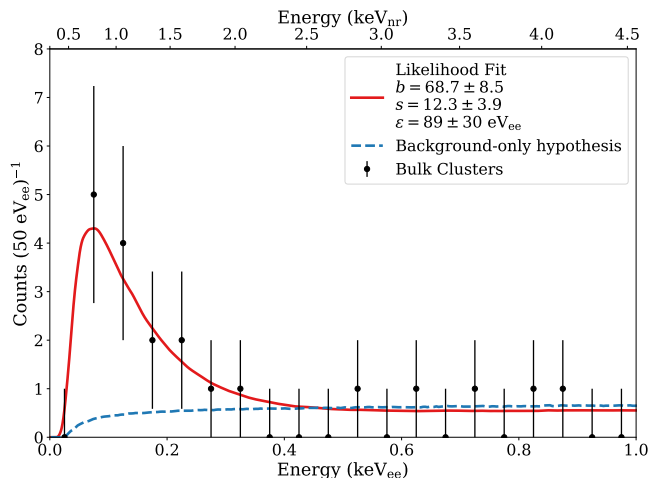


FIG. 3. Result of the fit to bulk events with the exponential excess + background (red) and the background-only (blue dashed) hypotheses. The fit prefers a low-energy exponential component. The top axis shows the nuclear recoil energy scale from CCD calibrations [14].

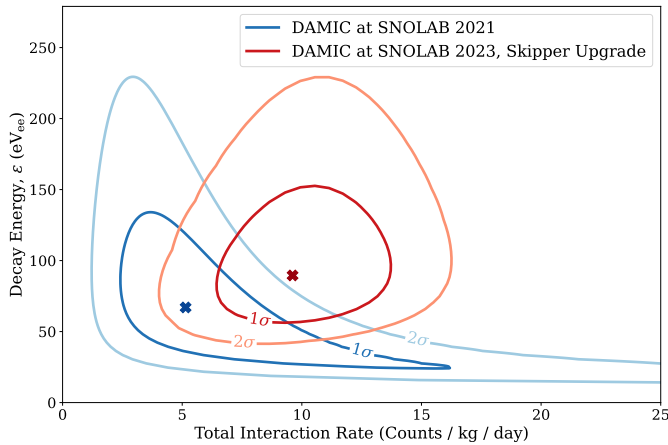


FIG. 4. Comparison of the allowed parameter space of the bulk excess measured in this work and the previous 11 kg-day analysis [2].

DAMIC-M detector [21], a 0.7 kg skipper-CCD array with an improved radioactive background rate of $\mathcal{O}(0.1) \text{ keV}_{\text{ee}}^{-1} \text{ kg}^{-1} \text{ day}^{-1}$, is scheduled to start operations at the Modane Underground Laboratory in late 2024. If the bulk excess is detected in SENSEI and DAMIC-M, the significantly increased statistics will enable a high-resolution spectral measurement, studies of the time evolution of the excess, and investigations of its dependence on detector configuration and operating parameters to better understand its origin.

ACKNOWLEDGMENTS

We are grateful to SNOLAB and its staff for support through underground space, logistical and technical services. SNOLAB operations are supported by the Canada Foundation for Innovation through the Major Science Initiatives Fund and the Province of On-

tario Ministry of Colleges and Universities, with underground access provided by Vale at the Creighton mine site. The DAMIC-M project has received funding from the European Research Council (ERC) under the European Union’s Horizon 2020 research and innovation programme Grant Agreement No. 788137, and from the U.S. National Science Foundation (NSF) through Grant No. NSF PHY-1812654. We thank the College of Arts and Sciences at the University of Washington for contributing the first CCDs to the DAMIC-M project. The CCD development at Lawrence Berkeley National Laboratory MicroSystems Lab was supported in part by the Director, Office of Science, of the U.S. Department of Energy under Contract No. DE-AC02-05CH11231. The SENSEI Collaboration is grateful for the support of the Heising-Simons Foundation under Grant No. 79921. We acknowledge financial support from the following agencies and organizations: NSF through Grant No. NSF PHY-2110585 to the University of Washington and The University of Chicago; the Kavli Institute for Cosmological Physics at The University of Chicago through an endowment from the Kavli Foundation; the U.S. Department of Energy Office of Science through the Dark Matter New Initiatives program; Fermi National Accelerator Laboratory (Contract No. DE-AC02-07CH11359); Institut Lagrange de Paris Laboratoire d’Excellence (under Reference No. ANR-10-LABX-63) supported by French state funds managed by the Agence Nationale de la Recherche within the Investissements d’Avenir program under Reference No. ANR-11-IDEX-0004-02; Swiss National Science Foundation through Grant No. 200021_153654 and via the Swiss Canton of Zurich; IFCA through project PID2019-109829GB-I00 funded by MCIN/AEI/10.13039/501100011033; Mexico’s Consejo Nacional de Ciencia y Tecnología (Grant No. CF-2023-I-1169) and Dirección General de Asuntos del Personal Académico–Universidad Nacional Autónoma de México (Programa de Apoyo a Proyectos de Investigación e Innovación Tecnológica Grant No. IN106322).

-
- [1] E. W. Kolb and M. S. Turner, *The Early Universe*, Vol. 69 (CRC Press, 1990).
 - [2] A. Aguilar-Arevalo *et al.* (DAMIC Collaboration), *Phys. Rev. Lett.* **125**, 241803 (2020), [arXiv:2007.15622 \[astro-ph.CO\]](#); *Phys. Rev. D* **105**, 062003 (2022), [arXiv:2110.13133 \[hep-ex\]](#).
 - [3] A. Piers, Ph.D. thesis, University of Washington (2023).
 - [4] I. Arnquist *et al.* (DAMIC-M Collaboration), *Phys. Rev. Lett.* **130**, 171003 (2023), [arXiv:2302.02372 \[hep-ex\]](#).
 - [5] S. Cebrián, *Int. J. Mod. Phys. A* **32**, 1743006 (2017), [arXiv:1708.07449 \[nucl-ex\]](#); L. Baudis, A. Kish, F. Piastra, and M. Schumann, *Eur. Phys. J. C* **75**, 485 (2015), [arXiv:1507.03792 \[astro-ph.IM\]](#).
 - [6] G. I. Canelo *et al.*, *J. Astron. Telesc. Instrum. Syst.* **7**, 015001 (2021), [arXiv:2004.07599 \[astro-ph.IM\]](#).
 - [7] S. E. Holland, D. E. Groom, N. P. Palaio, R. J. Stover, and M. Wei, *IEEE Trans. Electron. Dev.* **50**, 225 (2003).
 - [8] L. Barak *et al.* (SENSEI Collaboration), *Phys. Rev. Applied* **17**, 014022 (2022), [arXiv:2106.08347 \[physics.ins-det\]](#).
 - [9] J. Janesick, *Scientific Charge-coupled Devices*, Press Monograph Series (SPIE, 2001); K. Nordlund *et al.*, *J. Nucl. Mater.* **512** (2018), [10.1016/j.jnucmat.2018.10.027](#).
 - [10] D. Rodrigues *et al.*, *Nucl. Instrum. Meth. A* **1010**, 165511 (2021), [arXiv:2004.11499 \[physics.ins-det\]](#).
 - [11] A. Aguilar-Arevalo *et al.* (DAMIC Collaboration), *Phys. Rev. D* **94**, 082006 (2016), [arXiv:1607.07410 \[astro-ph.CO\]](#).
 - [12] G. Moroni Fernandez *et al.*, *Phys. Rev. Applied* **17**, 044050 (2022), [arXiv:2107.00168 \[hep-ex\]](#).
 - [13] D. Norcini *et al.* (DAMIC-M Collaboration), *Phys. Rev. D* **106**, 092001 (2022), [arXiv:2207.00809 \[physics.ins-det\]](#).

- det].
- [14] A. E. Chavarria *et al.*, *Phys. Rev. D* **94**, 082007 (2016), [arXiv:1608.00957 \[astro-ph.IM\]](#).
 - [15] K. Ramanathan *et al.*, *Phys. Rev. D* **96**, 042002 (2017), [arXiv:1706.06053 \[physics.ins-det\]](#).
 - [16] D. Baxter *et al.*, *Eur. Phys. J. C* **81**, 907 (2021), [arXiv:2105.00599 \[hep-ex\]](#).
 - [17] R. Agnese *et al.* (SuperCDMS Collaboration), *Phys. Rev. D* **99**, 062001 (2019), [arXiv:1808.09098 \[astro-ph.CO\]](#).
 - [18] P. Agnes *et al.* (DarkSide-50 Collaboration), *Phys. Rev. D* **107**, 063001 (2023), [arXiv:2207.11966 \[hep-ex\]](#).
 - [19] J. L. Feng, J. Kumar, D. Marfatia, and D. Sanford, *Phys. Lett. B* **703**, 124 (2011), [arXiv:1102.4331 \[hep-ph\]](#); in *Snowmass 2013: Snowmass on the Mississippi* (2013) [arXiv:1307.1758 \[hep-ph\]](#).
 - [20] L. Barak *et al.* (SENSEI), *Phys. Rev. Lett.* **125**, 171802 (2020), [arXiv:2004.11378 \[astro-ph.CO\]](#).
 - [21] I. Arnquist *et al.* (DAMIC-M Collaboration), in *14th International Workshop on the Identification of Dark Matter 2022* (2022) [arXiv:2210.12070 \[hep-ex\]](#).